Design Optimisation of C – Shaped Optical Fibre Sensor

Nazirah Mohd Razali[1], Sumiaty Ambran[1]*, Christopher Holmes[2], Siti Nur Fatin Zuikafly[1],

Muhammad Quisar Lokman[1], Ali Yuzir[2], Husni Hani Jameela Sapingi[1]

[1] Department of Electronic Systems Engineering, Malaysia – Japan International Institute of Technology, Universiti Teknologi Malaysia, 54000, Kuala Lumpur, Malaysia
[2] Optoelectronics Research Centre, University of Southampton, Southampton SO17 1BJ, UK.
[3] Department of Environmental Engineering and Green Technology, Malaysia – Japan International Institute of Technology, Universiti Teknologi Malaysia, 54100, Kuala Lumpur, Malaysia
*sumiaty.kl@utm.my

ABSTRACT— **Optical fibre sensors have attracted a lot of interest in the field of sensors. However, the limitation of conventional optical fibre sensors such as high fragility and low sensitivity need to be considered. This work demonstrated a simulation of a new optical sensor design, a C – shaped optical fibre sensor to overcome these limitations. The design optimization of the sensor was conducted by changing the remaining cladding thickness ranging from 5 – 0 µm and opening angle ranging from 70 – 110°. The change in refractive index ranging from 1.30 – 1.40 has been performed to evaluate the simulated sensing performance. The simulation results showed that reducing the cladding thickness and wider opening angle can improve the sensor's sensitivity. In cladding thickness optimization, the sensor showed the highest sensitivity with no remaining cladding thickness. In the opening angle optimization, the highest sensitivity can be achieved at the maximum opening angle of 110°, but the sensitivity changes due to the the opening angle range were minimal compared to cladding thickness optimization. The best C – shaped sensing performance with 0 µm remaining cladding thickness and 110° opening angle was selected to be compared to the closest in term of design which is the D – shaped optical fibre sensor. Overall, the C – shaped design has more cladding sector region left providing better physical robustness and has high potential to act as a new refractive index sensor with an estimated sensitivity of up to 2.77893 A.U, higher than the simulated D – shaped optical fibre sensor with an estimated sensitivity of 2.77468 A.U.**

Keywords—design, simulation, C - shaped, optical fibre sensor, refractive index

Introduction

Optical fibre sensor (OFS) refractometers have been widely demonstrated in measuring physical, chemical, and biological parameters, offering refractive index (RI) measurement for quality control and *in situ* monitoring. Generally, the target measurand can either be in the form of liquid, gas, or vapour, and its physical properties are measured based on the RI changes. The advantages of OFS includes pollution-free operation, corrosion resistance, remote sensing capability, immunity to electromagnetic interference, lightweight and small in size, high sensitivity, large bandwidth, and ease in light signal transmission (Joe et al., 2018; Qian et al., 2018; Giurgiutiu 2018). The OFS has been applied for measuring chemical and biochemical concentration (Zaca-Morán et al., 2018; Kadir et al., 2020; Zhu et al., 2020), adulterant traces (Singh, Ansari, and Raghuwanshi 2021; Singh, Iqbal Ansari, and Raghuwanshi 2020; Necochea-Chamorro et al., 2019), and relative humidity (Syuhada et al., 2020; Huang et al., 2018; Owji et al., 2021). (Agnarsson et al., 2009)

To fabricate this optical miniature sensor, a part of the optical fibre cladding is modified and replaced with target measurand. Tapered OFS as the most popular type has strong sensitivity performance in which the cladding layer is fully modified through a heat-pulling method (Korposh et al., 2019; Wei 2020; Moś et al., 2019) to have the evanescent field exposed and interact with the sensing medium. Other than that, etched OFS allows full cladding removal via wet chemical etching by using hydrofluoric (HF) acid (Zaca-Morán et al., 2018; Owji et al., 2021; Bag et al., 2020). However, for both cases, the small segment of the fibre becomes extremely thin after cladding modification, causing it to be fragile, making it hard to handle (Patil, Patil, and Ghosh 2020; Zhao et al., 2020; Ying et al., 2017). Works to integrate and ruggedize etched fibre has been reported using flame hydrolysis deposition (Gray et al., 2018; Holmes et al., 2018). However, The use of HF acid in etched OFS fabrication is extremely hazardous and extraordinary caution when using it is recommended (Ghandehari 2018).

To overcome these drawbacks, side–polished OFS has been introduced where one side of the fibre is polished to form a D – shaped structure by using a simple mechanical polishing method consisting of a motor-driven polishing wheel and abrasive paper (Luo et al., 2021). Despite the heightened mechanical stability from the cladding support as compared to tapered and etched OFS, experimental work has proved that it has lower sensitivity due to limited evanescent field exposure and typically limited interaction length. A study conducted by Dudus *et al.* showed that the D-shaped OFS has a sensitivity of around 10 times smaller than that of a tapered OFS of the same interaction length (Dudus, Blue, and Uttamchandani 2013). The D – shaped sensor sensitivity can be increased by multiplying the polished region but it will reduce the physical robustness of the sensor (Chen et al., 2010).

An early investigation of the C – shaped fibre structure was conducted by Wu *et al* (Wu et al., 2013). A pure silica tube with an inner diameter of 4 mm and an outer diameter of 12 mm is machined to create a lateral slot along the axial direction, resulting in a C – shaped preform. Then, the preform was drawn to a C – shaped fibre with an outer diameter of 145 μm and inner hollow diameter of 48 μm. The multimode C – shaped fibre was spliced to the polarization-maintaining photonic crystal fibre (PM – PCF) and the mentioned inner diameter is selected to cover the entire air–hole region of the PM – PCF. The same author also conducted a slightly different experiment where the same C – shaped fibre size was spliced to the SMF (Wu et al., 2014). Both experiments used the C – shaped fibre as a sensing region which is filled with the target sample for measurement. This initial work has shown the possibility of fabricating the C – shaped OFS and integrating the structure into an optical fibre sensing system.

In the latest work, Tan *et al.* fabricated the C – shaped sensor by using a single mode fibre (SMF) inscribed with fibre Bragg grating (FBG) to act as a temperature-insensitive refractometer (Tan et al., 2018). The C – shaped OFS is fabricated by direct machining in which a quarter portion of the cladding layer is cut off before it was tested in glycerin solution at RI ranges of 1.330-1.410, achieving a sensitivity of 1300pm/RIU. The C – shaped structure offers strong mechanical stability to support the sensor due to more remaining cladding sector compared to the conventional OFS. This work has proved the capabilities of the C-shaped sensor as a refractometer in line with other OFS designs.

Despite the limited available literature on this particular sensor design, its fabrication process and advantages as mentioned before have proven its feasibility as a new OFS design. In this paper, a C – shaped OFS is designed and simulated via wave optic module - COMSOL Multiphysics® software. Previous work has never reported the design optimization in terms of cladding thickness and opening angle. Thus, this study will examine the effect of both parameters on the sensitivity performance of the sensor. Furthermore, the electric field distribution throughout the sensor and effective RI changes at different analyte RI mediums are also studied and the underlying physics are discussed. Finally, the best simulated C – shaped OFS will be compared with the closest in term of design, D – shaped OFS, to analyse the sensing performance.

1. METHODOLOGY

The structure under investigation is illustrated in Fig. 1. It consists of SMF with core and cladding diameters of 9 µm and 125 µm, respectively. We chose to simulate SMF – based sensors because it tends to have higher sensitivity than their MMF counterparts (Dudus, Blue, and Uttamchandani 2013). Fig. 1(a) depicts the 3 – dimensional structure of the C – shaped OFS. To form the 'C' shape, about a quarter of the cladding structure was cut-off using a right triangle at the apex of 90° from the fibre centre (Tan et al., 2018). The cut-off region is then replaced with a sensing medium (analyte) for simulation purposes as shown in the cross-section view in Fig. 1(b). The design is firstly optimized at different cladding thicknesses ranging from 0 – 5 µm to access the penetration depth of the evanescent wave, after which the cladding thickness with the best performance is applied in the second optimization by adjusting the opening angle ranging from 70 – 110° to retain the 'C – shape' structure. The design optimization on cladding thickness and the opening angle is shown in the inset of Fig. 1(b).

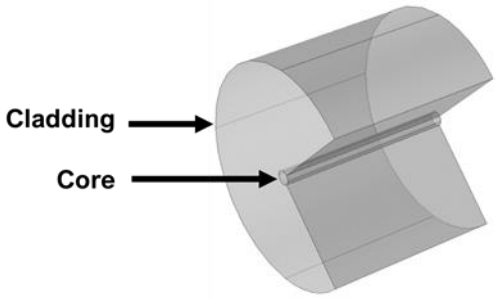

(a)

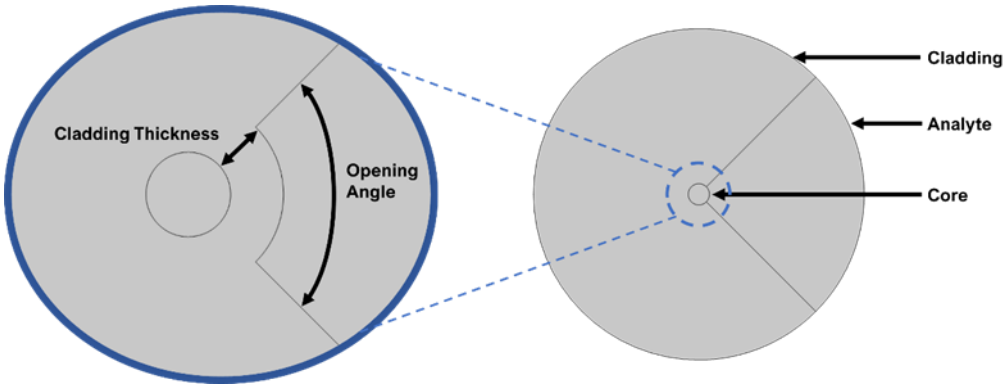

(b)

Fig. 1. The structure of C – shaped OFS in a) 3D and b) cross-section geometry for simulation purposes. The inset shows how the optimization is done on cladding thickness and opening angle

A three-term Sellmeier equation is used to express the SMF's RI at the near-infrared wavelength region as described in Eq. 1 (Khanikar and Singh 2019):

$$n(\lambda) = \sqrt{\frac{A_1\lambda^2}{\lambda^2 - \lambda_1^2} + \frac{A_2\lambda^2}{\lambda^2 - \lambda_2^2} + \frac{A_3\lambda^2}{\lambda^2 - \lambda_3^2} + 1} \quad (1)$$

Where n is the material RI and λ is the operating wavelength. Both core and cladding have different Sellmeier coefficients which are shown in the following Table 1:

Table 1: Sellmeier coefficient for simulation (Oh and Paek 2012; Brückner 2011):

Sellmeier Coefficient	A_1	A_2	A_3	λ_1	λ_2	λ_3
Core	0.6961663	0.4079426	0.8974794	0.0684043	0.1162414	9.896161
Cladding	0.7083925	0.4203993	0.8663412	0.0853842	0.1024839	9.896175

The simulation settings are summarized in Table 2. The sensing medium RI is set from 1.30 to 1.40, a typical range of a liquid RI used for OFS calibration (Chen et al., 2018; de Almeida et al., 2018). All the RI medium is set to isotropic. The SMF is made from glass and the analyte is assumed to be in the form of liquid, so they possess only one RI for all directions (Chipman, Lam, and Young 2018). 1550 nm is chosen as the operating wavelength where the lowest attenuation window of practical fibre is established (Green 2019).

Table 2: Simulation settings

Parameter	Expression / Settings	Value
Operating Wavelength	-	1550 nm
Core refractive index	Sellmeier Equation	1.4529 RIU
Cladding refractive index	Sellmeier Equation	1.4440 RIU
Liquid refractive index	-	1.30 – 1.40 (Step: 0.01) RIU
Refractive Index Medium	Isotropic	-

The C – shaped OFS has a similar working principle as D – shaped OFS (Tan et al., 2018). Changes in the sensor structure and the analyte medium will change the speed of light propagation in the sensor and in turn, changing the effective RI, n_{eff} value of the sensor. Numerically, the n_{eff} can be described as in Eq. 2 (Sukhoivanov and Guryev 2009):

$$n_{eff} = \frac{c}{v_g} \tag{2}$$

Where, c is the speed of light in a vacuum and v_g is the group velocity of light that propagates through the optical fibre. Now, the sensor depends on the interaction of the evanescent wave between the sensor and the analyte medium. The evanescent field 'senses' the changes in the RI distribution caused by the analyte medium, thus inducing the n_{eff} of the sensor. The evanescent wave will decay exponentially with a distance in the analyte medium and it is called penetration depth, d_p which can be expressed as in Eq. 2 (Agnarsson et al., 2009):

$$d_p = \frac{\lambda}{2\pi\sqrt{(n_{eff}^2 sin^2\theta - n_a^2)}} \tag{3}$$

Where, λ is the operating wavelength and n_a is the analyte RI. From Equation 2, the changes in n_a will change the d_p value. The RI of an unknown n_a medium can be easily detected by using this evanescent

wave interaction. Gao et al. claimed that the sensor sensitivity, S can be calculated by using Eq. 4 (Gao et al., 2014):

$$S = \frac{n_{eff}}{n_a} \frac{1}{\sqrt{n_{eff}^2 - n_a^2}} \tag{4}$$

The sensitivity can be increased to a very large value when n_a approaches n_{eff}. The sensor has a better sensing performance when n_a is closer to the n_{eff} (Gao et al., 2014). Hence, in this work, the maximum sensitivity of the sensor is studied at the highest analyte RI, 1.40, where the maximum sensitivity can be achieved.

2. RESULTS AND DISCUSSION

3.1 Electric Field Distribution and Sensor Sensitivity at Different Cladding Thickness

The simulation output is presented in two forms. Firstly, a coloured illustration of the electrical field intensity through the sensor structure helps in visualizing optical properties such as light propagation, the electric field distribution, light intensity, and evanescent wave. Secondly, a plotted graph to analyse the mode field diameter (MFD) and effective RI value of the simulated device.

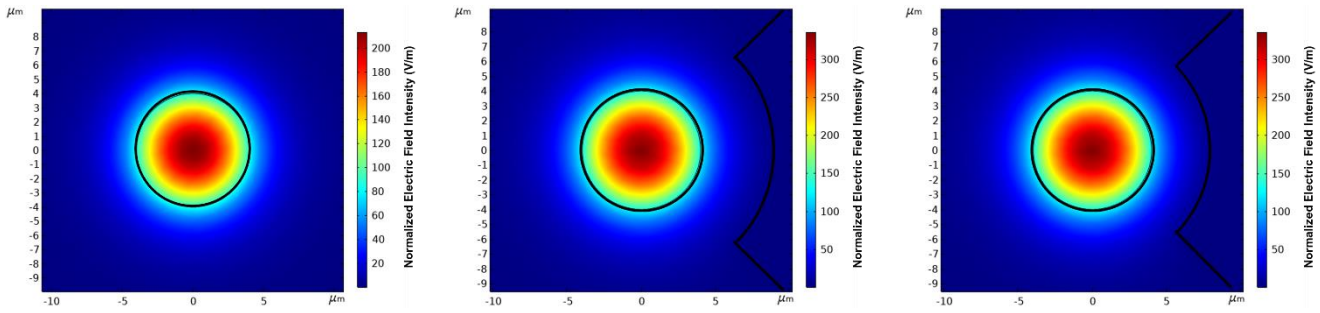

(a) (b) (c)

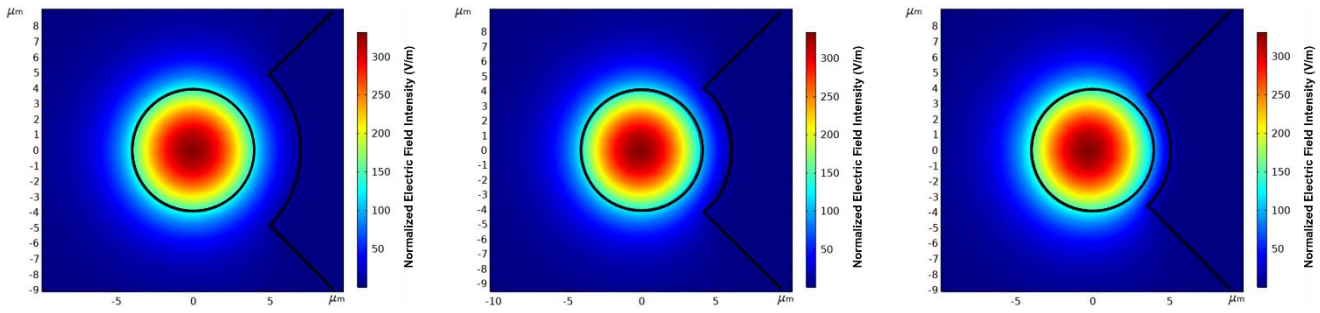

(d) (e) (f)

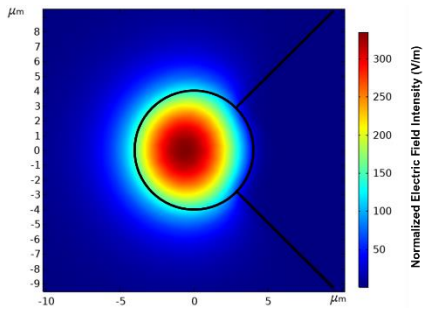

(g)

Fig. 2. Coloured illustration of normalized electric field intensity around the fiber core for (a) SMF and C – shaped with (b) 5 µm, (c) 4 µm, (d) 3 µm, (e) 2 µm, (f) 1 µm and (g) 0 µm of remaining cladding thickness when exposed to the analyte medium with RI of 1.33.

Fig. 2 shows the supported mode profile. In a selective study, the coloured illustration of the electric field distribution is illustrated through SMF and C – shaped sensors at different remaining cladding thicknesses ranging from 0 – 5 µm when exposed to the analyte RI at 1.33. The red and blue colour represents the maximum and the minimum electric field intensity. In the SMF structure, the electric field is concentrated at the centre and equally distributed indicating that the light is strongly confined in the core. However, when reducing the remaining cladding thickness, the electric field is slightly shifted towards the core/cladding boundary due to the lower RI contrast between these two mediums compared to the core/analyte boundary. The significant electric field shift can be seen when the remaining cladding thickness is reduced to 1 µm and 0 µm. For all cases, the colour faded out from red to blue showing that the electric field gradually decreases when reaching the core/cladding and core/analyte boundary due to the light energy attenuation as it reaches the boundary with different RI mediums.

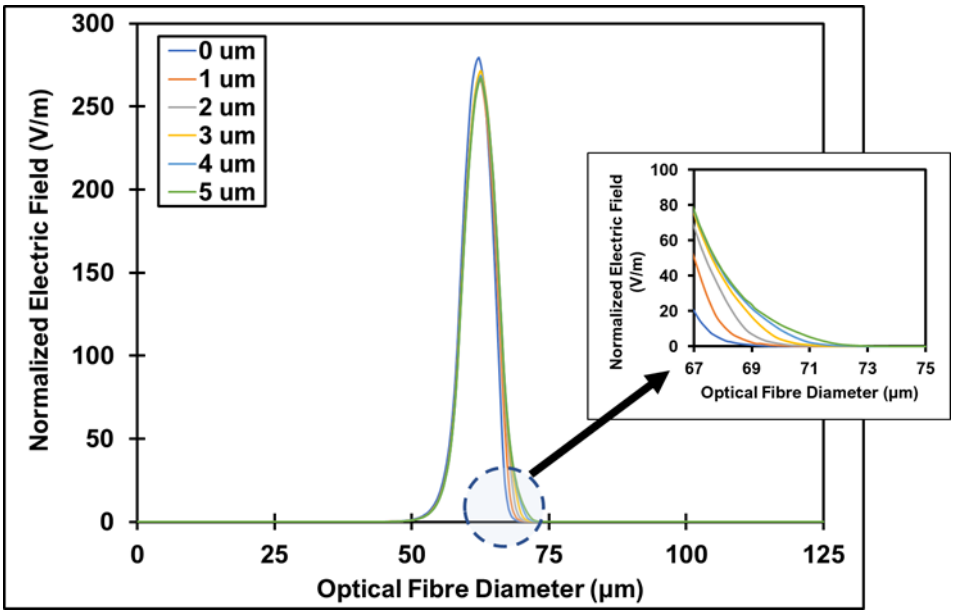
Normalized Electric Field (V/m)
Optical Fibre Diameter (μm)
0 um
1 um
2 um
3 um
4 um
5 um
Normalized Electric Field (V/m)
Optical Fibre Diameter (μm)

(a)

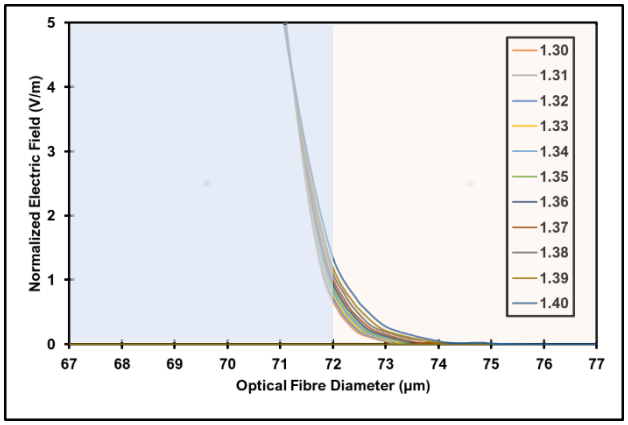
Normalized Electric Field (V/m)
Optical Fibre Diameter (μm)
1.30
1.31
1.32
1.33
1.34
1.35
1.36
1.37
1.38
1.39
1.40

(b)

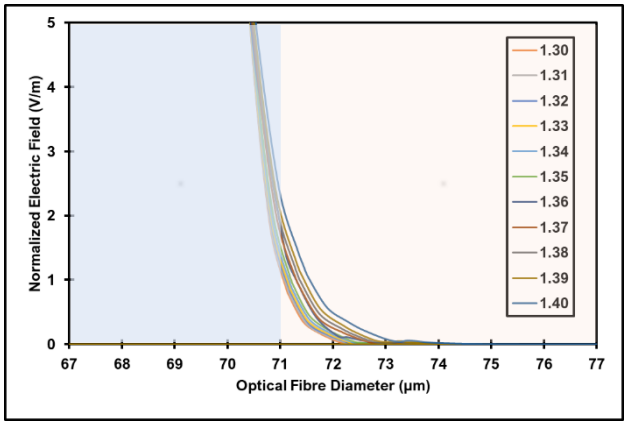
Normalized Electric Field (V/m)
Optical Fibre Diameter (μm)
1.30
1.31
1.32
1.33
1.34
1.35
1.36
1.37
1.38
1.39
1.40

(c)

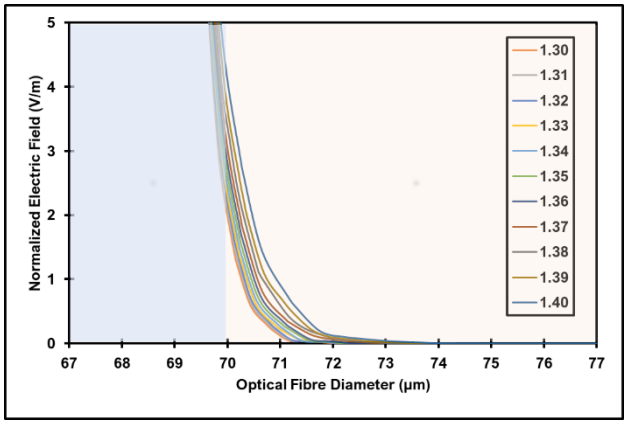
Normalized Electric Field (V/m)
Optical Fibre Diameter (μm)
1.30
1.31
1.32
1.33
1.34
1.35
1.36
1.37
1.38
1.39
1.40

(d)

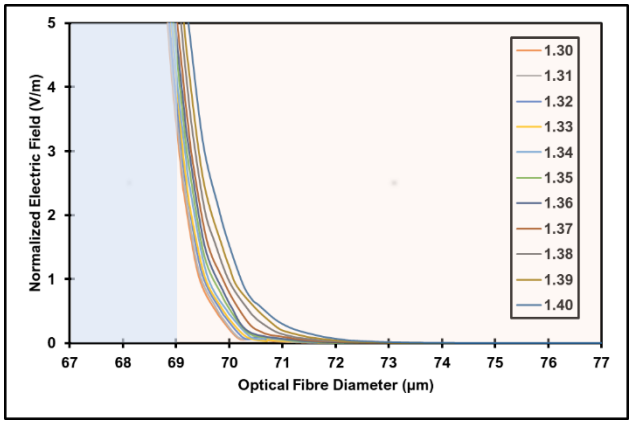
Normalized Electric Field (V/m)
Optical Fibre Diameter (μm)
1.30
1.31
1.32
1.33
1.34
1.35
1.36
1.37
1.38
1.39
1.40

(e)

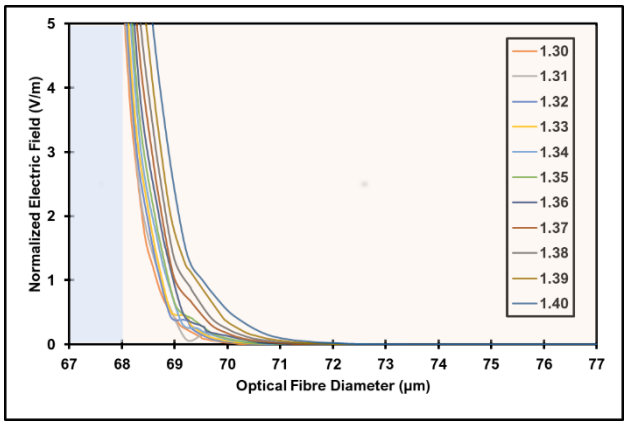

(f)

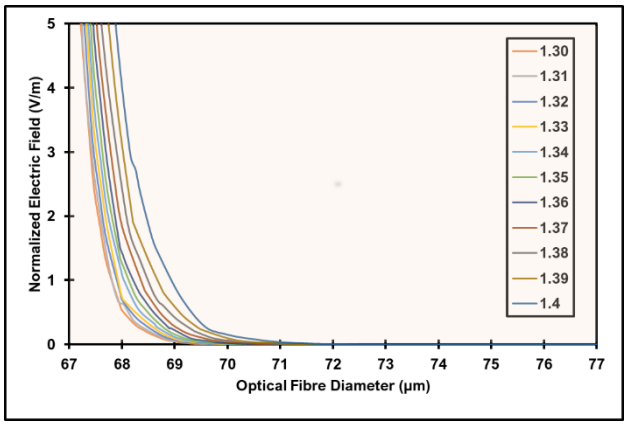

(g)

Fig. 3. (a) MFD of the C – shaped OFS at different cladding thickness at a selective analyte RI of 1.33. The inset shows the penetration depth at core/analyte boundary. Penetration depth for each thickness at different analyte RI is shown for (b) 5 µm, (c) 4 µm, (d) 3 µm, (e) 2 µm, (f) 1 µm, and (g) 0 µm. The initial value of 67 µm on the x-axis of the graph represents the core/cladding boundary. The blue region represents the thickness of the cladding layer, and the brown region represents the analyte medium

The electric field distribution of the C – shaped OFS can be analysed by studying the MFD as depicted in Fig. 3. A large variation of MFD can be seen when reducing the remaining cladding thickness from 5 – 0 µm as shown in Fig. 3(a). At the core/analyte boundary, the penetration depth of the evanescent wave decreases with the decrease in the cladding thickness. From the plotted graph in Fig. 3(b)-(g), the lowest penetration depth can be seen at 0 µm cladding thickness, with an estimated 4 µm of penetration depth and the highest penetration depth can be seen at 5 µm cladding thickness with an estimated 7 µm of penetration depth. It is worth mentioning that the penetration depth depends on the RI difference between the core, cladding and the analyte medium. By taking the core/cladding boundary as an example, the small RI difference between these two mediums causes a higher penetration depth probing further into the cladding medium. However, this condition may lead to a less sensitive sensor due to limited light interaction between the sensor and the analyte medium. In the case of 0 µm cladding thickness, although it has the smallest penetration depth due to high RI difference at the core/analyte boundary, the evanescent wave can fully

interact with the analyte medium thus increasing the sensor sensitivity. This explanation is summarized in Fig 4.

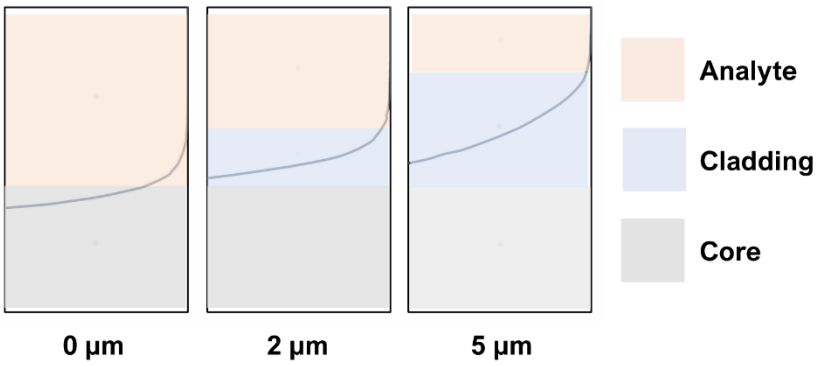

Fig. 4 Difference in penetration depth between 0 µm, 2 µm and 5 µm remaining cladding thickness. More evanescent wave interaction between sensor and analyte medium can be seen at 0 µm remaining cladding thickness compared to 2 µm and 5 µm The evanescent wave illustrated in this figure is the plotted MFD graph as shown in previous Fig. 3. Graph modification is made for illustration purposes.

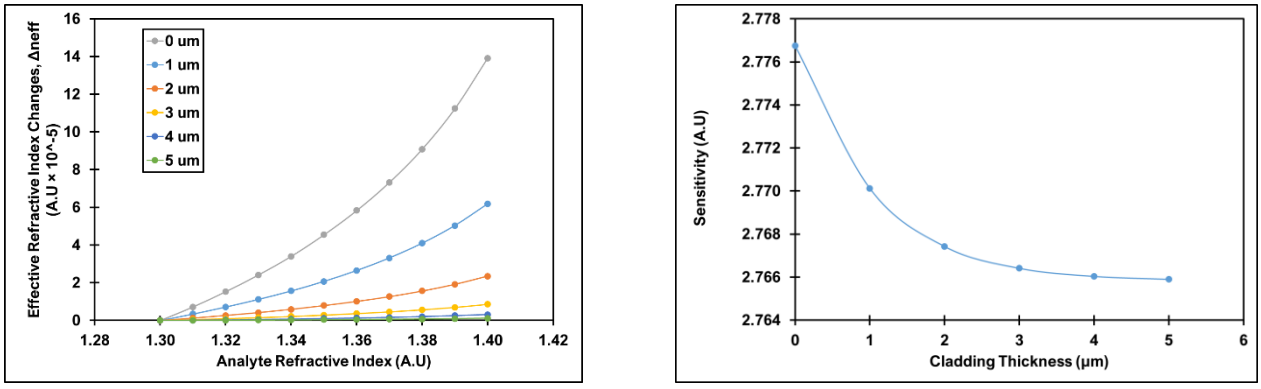

Fig. 5. (a) n_{eff} changes at different analyte RI and (b) sensor sensitivity of the C – shaped OFS at different remaining cladding thicknesses ranging from 0 – 5 µm

The registered n_{eff} changes for each cladding thickness are plotted at different analyte RI as shown in Fig. 5. As depicted in Fig. 5(a), as the analyte RI increases from 1.30 to 1.40, the n_{eff} changes also increases. There is an extremely small n_{eff} change occured at the 5 µm cladding thickness and the n_{eff} changes is

almost constant at a given analyte RI. However, the significant n_{eff} changes can be seen when reducing the cladding to the minimum of 0 µm thickness. Fig. 5(b) shows the sensitivity changes towards the cladding thickness calculated at the highest analyte RI of 1.40. It can be concluded that the C - shaped sensor at the remaining cladding thickness of 0 µm shows the highest estimated sensitivity of 2.77675 A.U and the remaining cladding thickness of 5 µm shows the smallest sensitivity of 2.76590 A.U, with total sensitivity changes of 0.01085 A.U. This is expected since the evanescent wave fully 'senses' the disturbance from the analyte medium when the cladding layer is removed, causing more light interaction between the sensor and analyte medium. In addtition, the simulation results are consistent with the simulation study conducted by (Kim et al., 2012) and the experimental study shown by Patil *et. al* (Patil, Saha, and Barma 2018) in which the sensitivity of the etched OFS increases when reducing the remaining cladding thickness.

3.2 Electric Field Distribution and Sensor Sensitivity at Different Opening Angle

The cladding thickness of the C – shaped OFS at 0 µm is selected to further study the effect of the opening angle on the sensor performance as the mentioned thickness provided the highest sensitivity on the cladding thickness optimization. Fig. 6 shows the simulation output as the light wave propagated through the fibre structure. In a selective study, the coloured illustration of the electric field distribution is illustrated through the C – shaped sensor at different opening angles ranging from 70 – 110° at analyte RI of 1.33. However, though hardly visible, there existed small changes in the electric field distribution at different opening angles. This observation can also be supported by analysing the MFD of the sensor.

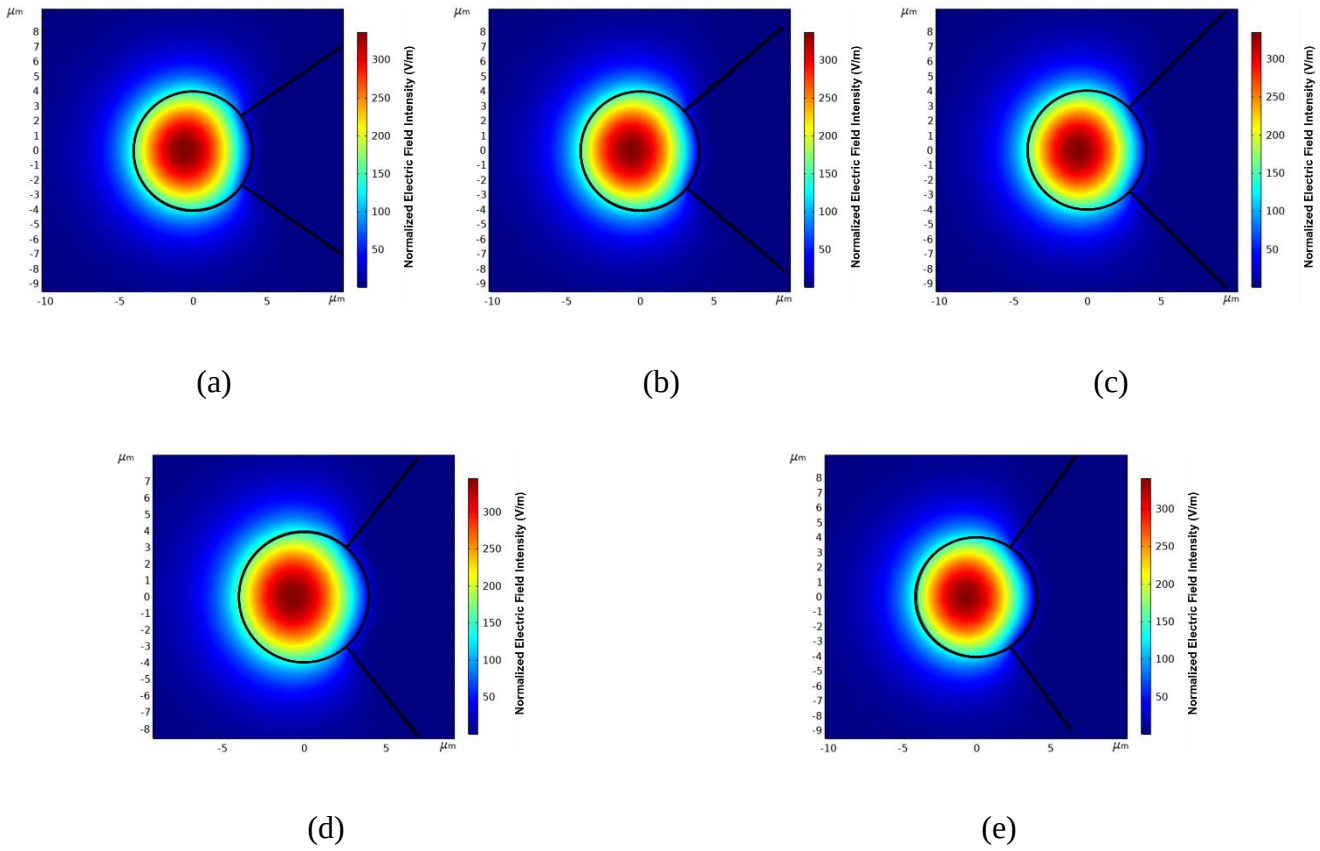

Fig. 6. Coloured illustration of normalized electric field intensity around the fibre core for C – shaped OFS at different opening angles when exposed to the analyte medium with RI of 1.33; (a) 70° (b) 80°, (c) 90°, (d) 100°, and (e) 110°

The MFD analysis of the C – shaped OFS at different opening angles is depicted in Fig. 7. As depicted from Fig. 7(a), the penetration depth for each opening angle ranging from 70 - 110° shows a small change. Fig. 7(b)-(f) represents the MFD at different analyte RI for each opening angle size. The penetration depth became smaller when opening angle increases. Although the penetration depth changes are very small as compared to that due to thickness optimization, the electric field distribution throughout the sensor can still differentiate the analyte RI without being overlapped. This can be supported by analysing the n_{eff} changes toward the analyte RI.

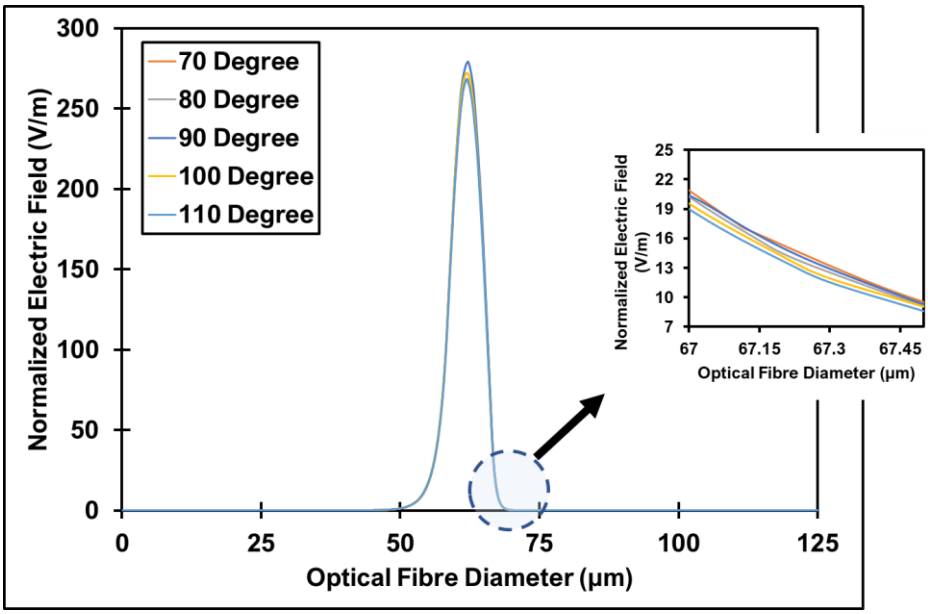
70 Degree
80 Degree
90 Degree
100 Degree
110 Degree
Normalized Electric Field (V/m)
Optical Fibre Diameter (µm)
Normalized Electric Field (V/m)
Optical Fibre Diameter (µm)

(a)

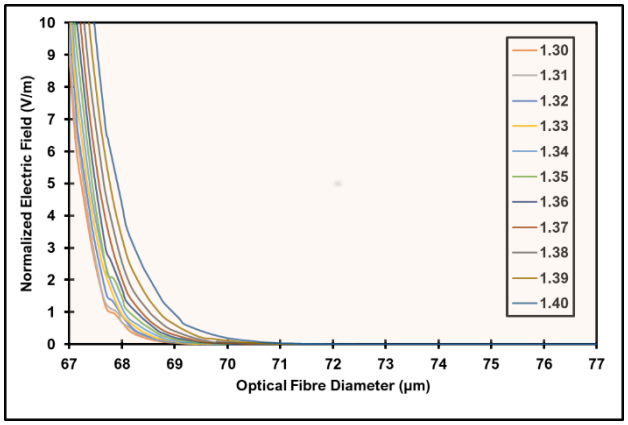
1.30
1.31
1.32
1.33
1.34
1.35
1.36
1.37
1.38
1.39
1.40
Normalized Electric Field (V/m)
Optical Fibre Diameter (µm)

(b)

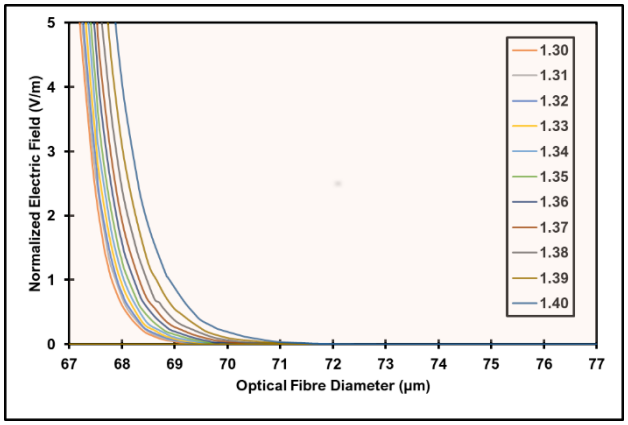
1.30
1.31
1.32
1.33
1.34
1.35
1.36
1.37
1.38
1.39
1.40
Normalized Electric Field (V/m)
Optical Fibre Diameter (µm)

(c)

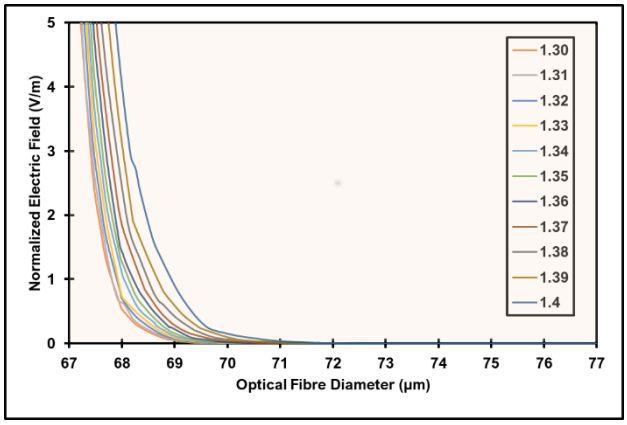
1.30
1.31
1.32
1.33
1.34
1.35
1.36
1.37
1.38
1.39
1.4
Normalized Electric Field (V/m)
Optical Fibre Diameter (µm)

(d)

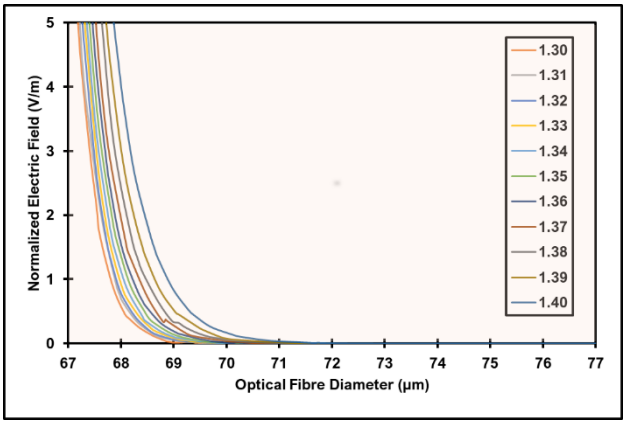
1.30
1.31
1.32
1.33
1.34
1.35
1.36
1.37
1.38
1.39
1.40
Normalized Electric Field (V/m)
Optical Fibre Diameter (µm)

(e)

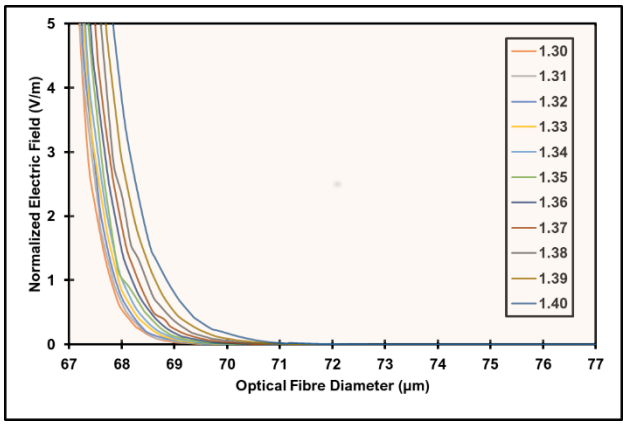

(f)

Fig. 7. MFD of the C – shaped OFS (a) at different opening angles. Penetration depth for each opening at different analyte RI is shown in (b) 70°, (c) 80°, (d) 90°, (e) 100°, and (f) 110°,

The registered n_{eff} changes for each opening angle are plotted at different analyte RI as shown in Fig. 8. As the analyte RI increases from 1.30 to 1.40, the n_{eff} also increases. For all cases, the C – shaped OFS at different opening angles can interact well with the analyte medium by giving different n_{eff} changes at different analyte RI. The smallest and highest change can be seen at 70° and 110° of opening angle, respectively. Fig. 7(b) summarizes the sensitivity performance towards the opening angle. The sensitivity linearly increased when increasing the opening angle. At 70° of opening angle, the sensor achieved the smallest estimated sensitivity of 2.77893 A.U but the highest estimated sensitivity of 2.77468 A.U is achieved at 110° which results in the highest analyte RI of 1.40 with the total sensitivity changes from 70 - 110° of 0.00425 A.U. As the opening angle becomes wider, such condition will increase the area of evanescent field exposure onto the analyte medium, thus, increasing the interaction between the sensor and the analyte medium. The simulation is also supported by the previous work, where the degree of the evanescent field exposure will affect the sensing interaction as claimed by the author (Dudus, Blue, and Uttamchandani 2013).

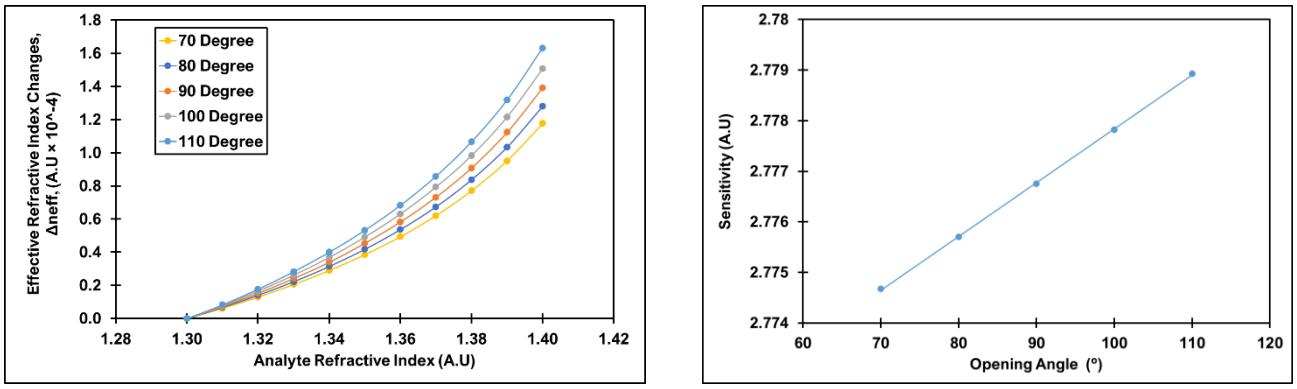

Fig. 8. n_{eff} at different analyte RI for C – shaped OFS at different opening angles ranging from 70 – 110°

3.3 Overall C – Shaped Sensing Performance and Comparison with D – Shaped Optical Fibre Sensor

Based on this simulation work, the C – shaped sensor has a high possibility for RI measurement. The sensing performance is improved when the remaining cladding thickness is reduced. Without a cladding layer, the sensor shows the highest sensitivity performance. In addition, the greater the opening angle of the C – shaped sensor, the more sensitive the sensor becomes. However, based on these findings, increasing the opening angle can only increase the sensor sensitivity by a small degree compared to cladding thickness reduction which shows more significant sensitivity changes. The overall C – shaped sensing performance is summarized in Table 3.

Table 3. Simulated sensor performance of C-shaped at different optimized parameter

Optimized Parameter	Sensitivity (A.U)	Total Sensitivity Changes (A.U)
Cladding Thickness		
Highest sensitivity = 0 µm	2.77675	0.01085
Lowest sensitivity = 5 µm	2.76590	

Opening Angle		
Lowest sensitivity = 70°	2.77893	0.00425
Highest sensitivity = 110°	2.77468	

The sensor performance in term of sensitivity is compared between two OFS design which is the C – shaped and the D-shaped OFS for their close similarity in design. The C – shaped OFS at 0 µm and 110° opening angle is selected for this purpose. The D – shaped OFS is simulated with the same simulation settings as mentioned before, without remaining cladding thickness. Fig. 9(a) depicts the sensing comparison between the C – shaped and D – shaped OFS. The estimated sensitivity achieved by the C - shaped OFS is 2.77893 A.U, higher than the D - shaped OFS, with an estimated sensitivity of 2.77620 A.U which results in the highest analyte RI of 1.40. This is expected since the evanescent wave exposure area of C – shaped is better than D – shaped OFS. Both simulated sensor performance is summarized in Table 4. Furthermore, the C – shaped design has more cladding sector region left to support the physical robustness of the sensor compared to D-shaped OFS, promising a more reliable sensor design as illustrated in Fig. 9(b).

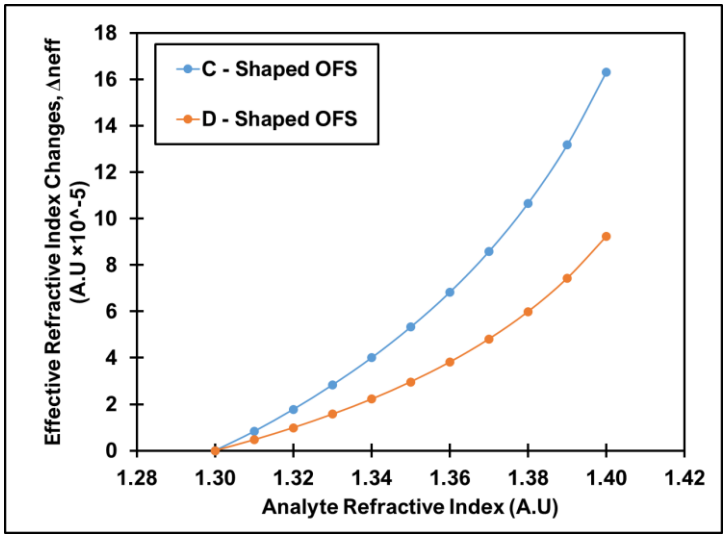

(a)

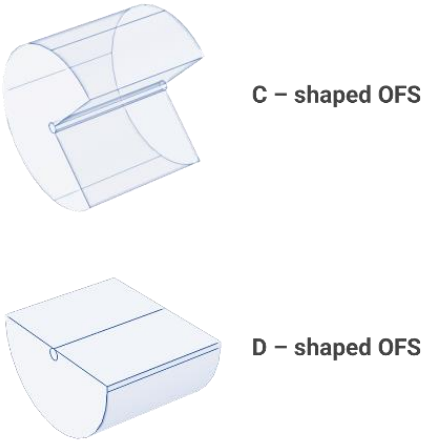

(b)

Fig. 9. (a) n_{eff} changes of the best simulated C – shaped and D - shaped OFS at different analyte RI and (b) the comparison structure between the two sensors in remaining cladding sector region.

Table 4. Simulated sensor performance of C-shaped and D-shaped OFS

Type of Simulated OFS	**Sensitivity (A.U)**
C – shaped	2.77893
D - shaped	2.77620

Conclusion

This work demonstrated the design and simulation of C – shaped OFS at different analyte RI ranging from 1.30 – 1.40. The conducted design optimization at different cladding thicknesses and opening angles is greatly helpful in determining the best C – shaped OFS sensitivity. In the simulation evaluation, the optimized C – shaped sensor measuring the different analyte RI shows different electric field distribution and evanescent field without being overlapped. The highest estimated sensitivity achieved by the C - shaped sensor is 2.77893 A.U with 0 μm of cladding thickness and 110° of opening angle. This sensitivity is higher than the simulated D – shaped OFS with an estimated sensitivity of 2.77620 A.U. The simulated design evinced C-shaped design as a convincing one for a new OFS type.

Authors' contributions: Conceptualization: Nazirah Mohd Razali; Methodology: Nazirah Mohd Razali and Sumiaty Ambran; Formal analysis and investigation: Nazirah Mohd Razali, Muhammad Quisar Lokman, Christopher Holmes and Sumiaty Ambran; Writing - original draft preparation: Nazirah Mohd Razali and Siti Nur Fatin Zuikafly; Writing - review and editing: Siti Nur Fatin Zuikafly, Muhammad Quisar Lokman, and Sumiaty Ambran; Funding Acquisition: Ali Yuzir; Supervision: Sumiaty Ambran. Christopher Holmes and Husni Hani Jameela Sapingi

Conflict of interests: The authors declare that they have no conflict of interest.

Consent to participate: The authors give their consent to participate.

Consent to publishing: The authors give their consent to publish.

REFERENCES

Agnarsson, Björn, Saevar Ingthorsson, Thorarinn Gudjonsson, and Kristjan Leosson. 2009. 'Evanescent-wave fluorescence microscopy using symmetric planar waveguides', *Optics Express*, 17: 5075-82, DOI:https://doi.org/10.1364/OE.17.005075.

Bag, Saawan K., Meher Wan, Rajat K. Sinha, and Shailendra K. Varshney. 2020. 'Design and characterization of surface relief grating on etched multimode optical fiber for refractive index sensing', *Sensors and Actuators A: Physical*, 303: 111836, DOI:https://doi.org/10.1016/j.sna.2020.111836.

Brückner, Volkmar. 2011. 'To the use of Sellmeier formula', *Senior Experten Service (SES) Bonn and HfT Leipzig, Germany*, 42: 242-50.

Chen, C. H., T. C. Tsao, J. L. Tang, and W. T. Wu. 2010. 'A multi-D-shaped optical fiber for refractive index sensing', *Sensors (Basel)*, 10: 4794-804, DOI:https://doi.org/10.3390/s100504794.

Chen, Chao, Rui Yang, Xuan-yu Zhang, Wei-hua Wei, Qi Guo, Xing Zhang, Li Qin, Yong-qiang Ning, and Yong-sen Yu. 2018. 'Compact refractive index sensor based on an S-tapered fiber probe', *Optical Materials Express*, 8: 919-25, DOI:https://doi.org/10.1364/OME.8.000919.

Chipman, Russell A, Wai-Sze Tiffany Lam, and Garam Young. 2018. *Polarized light and optical systems* (CRC press).

de Almeida, Jmmm, H. Vasconcelos, P. A. S. Jorge, and L. Coelho. 2018. 'Plasmonic Optical Fiber Sensor Based on Double Step Growth of Gold Nano-Islands', *Sensors (Basel)*, 18: 1267, DOI:https://doi.org/10.3390/s18041267.

Dudus, Anna, Robert Blue, and Deepak Uttamchandani. 2013. 'Comparative Study of Microfiber and Side-Polished Optical Fiber Sensors for Refractometry in Microfluidics', *IEEE Sensors Journal*, 13: 1594-601, DOI:https://doi.org/10.1109/JSEN.2013.2239639.

Gao, F., H. Liu, C. Sheng, C. Zhu, and S. N. Zhu. 2014. 'Refractive index sensor based on the leaky radiation of a microfiber', *Opt Express*, 22: 12645-52, DOI:https://doi.org/10.1364/OE.22.012645.

Ghandehari, Masoud. 2018. 'Optical Waveguides.' in, *Optical Phenomenology and Applications* (Springer).

Giurgiutiu, Victor. 2018. '7.19 Smart Materials and Health Monitoring of Composites.' in Peter W. R. Beaumont and Carl H. Zweben (eds.), *Comprehensive Composite Materials II* (Elsevier: Oxford).

Gray, A. C., A. Jantzen, P. C. Gow, D. H. Smith, C. B. E. Gawith, P. G. R. Smith, and C. Holmes. 2018. 'Leaky mode integrated optical fibre refractometer', *Opt Express*, 26: 9155-64, DOI:https://doi.org/10.1364/OE.26.009155.

Green, Lynne D. 2019. *Fiber Optic Communications* (CRC Press).

Holmes, C., A. Jantzen, A. C. Gray, P. C. Gow, L. G. Carpenter, R. H. S. Bannerman, J. C. Gates, and P. G. R. Smith. 2018. 'Evanescent field refractometry in planar optical fiber', *Opt Lett*, 43: 791-94, DOI:https://doi.org/10.1364/OL.43.000791.

Huang, Yaoming, Wenguo Zhu, Zhibin Li, Guanglei Chen, Liheng Chen, Junjie Zhou, Hai Lin, Junwen Guan, Wenxiao Fang, Xin Liu, Huazhuo Dong, Jieyuan Tang, Heyuan Guan, Huihui Lu, Yi Xiao, Jun Zhang, Hongcheng Wang, Zhe Chen, and Jianhui Yu. 2018. 'High-performance fibre-optic humidity sensor based on a side-polished fibre wavelength selectively coupled with graphene oxide film', *Sensors and Actuators B: Chemical*, 255: 57-69, DOI:https://doi.org/10.1016/j.snb.2017.08.042.

Joe, Hang-Eun, Huitaek Yun, Seung-Hwan Jo, Martin BG Jun, and Byung-Kwon Min. 2018. 'A review on optical fiber sensors for environmental monitoring', *International journal of precision engineering and manufacturing-green technology*, 5: 173-91, DOI:https://doi.org/10.1007/s40684-018-0017-6.

Kadir, Nur Ameelia Abdul, Ninik Irawati, Afiq Arif Aminuddin Jafry, Nazirah Mohd Razali, Azura Hamzah, and Sulaiman Wadi Harun. 2020. 'Sodium nitrate sensor based on D-shaped fiber structure', *Measurement*, 163: 107927, DOI:https://doi.org/10.1016/j.measurement.2020.107927.

Khanikar, Tulika, and Vinod Kumar Singh. 2019. 'Gold grating assisted SPR based D-shaped single mode fiber for detection of liquid refractive index', *Optical and Quantum Electronics*, 51: 296, DOI:https://doi.org/10.1007/s11082-019-2013-7.

Kim, Kwang Taek, In Soo Kim, Cherl-Hee Lee, and Jonghun Lee. 2012. 'A temperature-insensitive cladding-etched fiber Bragg grating using a liquid mixture with a negative thermo-optic coefficient', *Sensors*, 12: 7886-92, DOI:https://doi.org/10.3390/s120607886.

Korposh, S., S. W. James, S. W. Lee, and R. P. Tatam. 2019. 'Tapered Optical Fibre Sensors: Current Trends and Future Perspectives', *Sensors (Basel)*, 19: 2294, DOI:https://doi.org/10.3390/s19102294.

Luo, Wei, Jinwei Meng, Xuejin Li, Qingli Xie, Duo Yi, Yanyong Wang, and Xueming Hong. 2021. 'Temperature effects on surface plasmon resonance sensor based on side-polished D-shaped photonic crystal fiber', *Measurement*, 181: 109504, DOI:https://doi.org/10.1016/j.measurement.2021.109504.

Moś, Joanna E, Joanna Korec, Karol A Stasiewicz, Bartłomiej Jankiewicz, Bartosz Bartosewicz, and Leszek R Jaroszewicz. 2019. 'Research on optical properties of tapered optical fibers with liquid crystal cladding doped with gold nanoparticles', *Crystals*, 9: 306, DOI:https://doi.org/10.3390/cryst9060306.

Necochea-Chamorro, Jorge Isaac, Roberto Carlos Carrillo-Torres, Raúl Sánchez-Zeferino, and Mario Enrique Álvarez-Ramos. 2019. 'Fiber optic sensor using ZnO for detection of adulterated tequila with methanol', *Optical Fiber Technology*, 52: 101982, DOI:https://doi.org/10.1016/j.yofte.2019.101982.

Oh, Kyunghwan, and Un-Chul Paek. 2012. *Silica optical fiber technology for devices and components: design, fabrication, and international standards* (John Wiley & Sons).

Owji, E., H. Mokhtari, F. Ostovari, B. Darazereshki, and N. Shakiba. 2021. '2D materials coated on etched optical fibers as humidity sensor', *Sci Rep*, 11: 1771, DOI:https://doi.org/10.1038/s41598-020-79563-w.

Patil, J. J., Y. H. Patil, and A. Ghosh. Comprehensive and Analytical Review on Optical Fiber Refractive Index Sensor. *2020 4th International Conference on Trends in Electronics and Informatics (ICOEI)(48184)* 2020, DOI:https://doi.org/10.1109/ICOEI48184.2020.9142916.

Patil, S. H., A. Saha, and M. Deb Barma. Performance Analysis of Cladding Etched Fiber Bragg Grating based Refractive Index Sensor. *2018 2nd International Conference on Electronics, Materials Engineering & Nano-Technology (IEMENTech)* 2018, DOI:https://doi.org/10.1109/IEMENTECH.2018.8465251.

Qian, Yu, Yong Zhao, Qi-lu Wu, and Yang Yang. 2018. 'Review of salinity measurement technology based on optical fiber sensor', *Sensors and Actuators B: Chemical*, 260: 86-105, DOI:https://doi.org/10.1016/j.snb.2017.12.077.

Singh, Yadvendra, Md Tauseef Iqbal Ansari, and Sanjeev Kumar Raghuwanshi. 2021. 'Design and Development of Titanium Dioxide (TiO_2)-Coated eFBG Sensor for the Detection of Petrochemicals Adulteration', *IEEE Transactions on Instrumentation and Measurement*, 70: 1-8, DOI:https://doi.org/10.1109/TIM.2021.3053985.

Singh, Yadvendra, Md Tauseef Iqbal Ansari, and Sanjeev Kumar Raghuwanshi. 2020. *Fuel adulteration detection system using etched clad based Fiber Bragg Grating (FBG) sensor* (SPIE).

Sukhoivanov, Igor A, and Igor V Guryev. 2009. *Photonic crystals: physics and practical modeling* (Springer).

Syuhada, Aneez, Muhammad Salleh Shamsudin, Suzairi Daud, Ganesan Krishnan, Sulaiman Wadi Harun, and Muhammad Safwan Abd Aziz. 2020. 'Single-mode modified tapered fiber structure functionalized with GO-PVA composite layer for relative humidity sensing', *Photonic Sensors*: 1-11, DOI:https://doi.org/10.1007/s13320-020-0595-0.

Tan, R. X., D. Ho, C. H. Tse, Y. C. Tan, S. W. Yoo, S. C. Tjin, and M. Ibsen. 2018. 'Birefringent Bragg Grating in C-Shaped Optical Fiber as a Temperature-Insensitive Refractometer', *Sensors (Basel)*, 18: 3285, DOI:https://doi.org/10.3390/s18103285.

Wei, Lei. 2020. *Advanced Fiber Sensing Technologies* (Springer).

Wu, C., Z. Liu, A. P. Zhang, B. O. Guan, and H. Y. Tam. 2014. 'In-line open-cavity Fabry-Perot interferometer formed by C-shaped fiber fortemperature-insensitive refractive index sensing', *Opt Express*, 22: 21757-66, DOI:https://doi.org/10.1364/OE.22.021757.

Wu, C., M. L. Tse, Z. Liu, B. O. Guan, C. Lu, and H. Y. Tam. 2013. 'In-line microfluidic refractometer based on C-shaped fiber assisted photonic crystal fiber Sagnac interferometer', *Opt Lett*, 38: 3283-6, DOI:https://doi.org/10.1364/OL.38.003283.

Ying, Yu, Guang-yuan Si, Fang-jun Luan, Ke Xu, Yuan-wei Qi, and Hong-nan Li. 2017. 'Recent research progress of optical fiber sensors based on D-shaped structure', *Optics & Laser Technology*, 90: 149-57, DOI:https://doi.org/10.1016/j.optlastec.2016.11.021.

Zaca-Morán, P., J. P. Padilla-Martínez, J. M. Pérez-Corte, J. A. Dávila-Pintle, J. G. Ortega-Mendoza, and N. Morales. 2018. 'Etched optical fiber for measuring concentration and refractive index of sucrose solutions by evanescent waves', *Laser Physics*, 28: 116002, DOI:https://doi.org/10.1088/1555-6611/aad846.

Zhao, Y., X. G. Hu, S. Hu, and Y. Peng. 2020. 'Applications of fiber-optic biochemical sensor in microfluidic chips: A review', *Biosens Bioelectron*, 166: 112447, DOI:https://doi.org/10.1016/j.bios.2020.112447.

Zhu, Guo, Niteshkumar Agrawal, Ragini Singh, Santosh Kumar, Bingyuan Zhang, Chinmoy Saha, and Chandrakanta Kumar. 2020. 'A novel periodically tapered structure-based gold nanoparticles and graphene oxide – Immobilized optical fiber sensor to detect ascorbic acid', *Optics & Laser Technology*, 127: 106156, DOI:https://doi.org/10.1016/j.optlastec.2020.106156.